Nanoscale

PAPER

View Article Online
View Journal | View Issue

Cite this: *Nanoscale*, 2016, **8**, 11099

The artificial control of enhanced optical processes in fluorescent molecules on high-emittance metasurfaces†

Masanobu Iwanaga,* Bongseok Choi,‡ Hideki T. Miyazaki and Yoshimasa Sugimoto

Plasmon-enhanced optical processes in molecules have been extensively but individually explored for Raman scattering, fluorescence, and infrared light absorption. In contrast to recent progress in the interfacial control of hot electrons in plasmon–semiconductor hybrid systems, plasmon–molecule hybrid systems have remained to be a conventional scheme, mainly assuming electric-field enhancement. This was because it was difficult to control the plasmon–molecule interface in a well-controlled manner. We here experimentally substantiate an obvious change in artificially enhanced optical processes of fluorescence/Raman scattering in fluorescent molecules on high-emittance plasmo-photonic metasurfaces with/without a self-assembled monolayer of sub-nm thickness. These results indicate that the enhanced optical processes were successfully selected under artificial configurations without any additional chemical treatment that modifies the molecules themselves. Although Raman-scattering efficiency is generally weak in high-fluorescence-yield molecules, it was found that Raman scattering becomes prominent around the molecular fingerprint range on the metasurfaces, being enhanced by more than 2000 fold at the maximum for reference signals. In addition, the highly and uniformly enhancing metasurfaces are able to serve as two-way functional, reproducible, and wavelength-tunable platforms to detect molecules at very low densities, being distinct from other platforms reported so far. The change in the enhanced signals suggests that energy diagrams in fluorescent molecules are changed in the configuration that includes the metal–molecule interface, meaning that plasmon–molecule hybrid systems are rich in the phenomena beyond the conventional scheme.

Received 16th February 2016,
Accepted 27th April 2016

DOI: 10.1039/c6nr01318j

www.rsc.org/nanoscale

1. Introduction

Plasmon enhancement is moving to a new phase beyond the previous scheme relying on simple electric(*E*)-field enhancement. Several papers reported that hot electrons contribute to electronic transitions in metal–semiconductor hybrid systems.[1–4] One of the key factors was found to be precise interface control. Similarly, the interplay between metallic nanostructures, which are now often referred to as plasmonic structures, and molecules has been expected to induce cooperative phenomena in a controllable manner. However, such phenomena have not yet been demonstrated experimentally though enhanced optical signals from molecules on plasmonic structures have been extensively investigated since the 1970s.[5–8] There are two main enhanced signals: Raman scattering[9–11] and fluorescence (FL).[12,13] The enhanced Raman scattering is also known as surface-enhanced Raman scattering (SERS). Although the two signals are induced *via* similar optical transitions in terms of energy diagrams of FL molecules, they have been mostly explored individually. As for the electron transfer to molecules, a recent study reported it in Au-atom-cluster–molecule hybrid systems,[14] in which discrete Au atoms directly couple with the molecules and do not form plasmonic (or collective excitation) states.

Conventionally, SERS signals were obtained using an additional chemical treatment such that chloride or bromide ions were added to the solutions to reduce FL and increase Raman signals.[9,15,16] However, such a treatment affects molecular states and modifies the molecules themselves. Therefore, to establish reliable molecular sensing techniques, it is preferable to detect molecules as they are without any additional treatment; generally, it is uncertain that such an additional chemical treatment is valid for diverse target molecules.

National Institute for Materials Science (NIMS), 1-1 Namiki, Tsukuba 305-0044, Japan. E-mail: iwanaga.masanobu@nims.go.jp

†Electronic supplementary information (ESI) available: Details of UV NIL and optical measurement are described, and the additional measured and numerical data are provided. See DOI: 10.1039/C6NR01318J

‡Present address: Materials & Devices Advanced Research Institute, LG Electronics, Seoul, South-Korea.

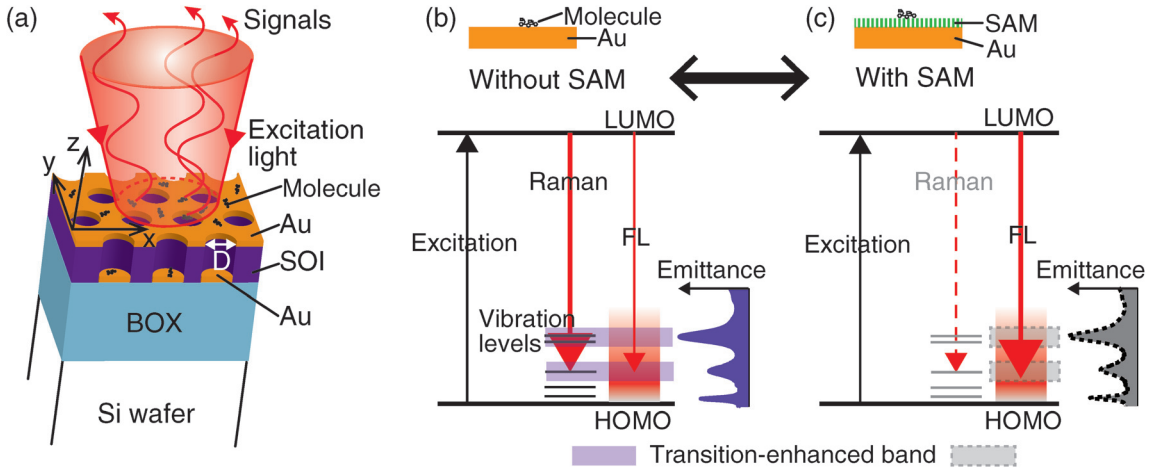

Fig. 1 Schematic illustrations of this study. (a) SC PlasPh metasurface and illumination-collection configuration. (b) and (c) Energy diagrams of FL molecules on the SC metasurfaces in the cases without and with a SAM, respectively. Resonant excitation results in the two distinct optical processes in (b) and (c), originating only from the SAM; the other conditions are equivalent to each other. Emittance of the SC metasurfaces, equal to absorbance, is also shown in accordance with the optical transitions in the molecules. Shadows (pale purple and gray) in the diagrams represent a transition-enhanced band due to the configuration interaction.

Furthermore, SERS signals reported so far were very sensitive to the so-called hot spots, which are locally intense *E*-field spots;[10,11,17–20] consequently, the reproduction of highly enhanced signals is not generally guaranteed, implying that the hot spots are very hard to control in reality. Thus, homogeneous SERS-signal detection is quite important for reliable sensing.[21–24] On the present metasurface platforms, which are artificial surface structures and new types of sensing platforms, the detected optical signals were found to be highly enhanced and simultaneously quite uniform; indeed, we have not observed any significant difference in the spot-to-spot measurements and did estimate the difference to be at most 5%.

Recently, further advances in SERS[25,26] and enhanced FL studies[13,27,28] have focused on the actual application for biosensing. For the more reliable sensing techniques, it would be preferable that sensing platforms are capable of detecting both Raman scattering and FL to securely identify the molecular species. However, such multi-functional platforms have not been introduced.

We here show that the two enhanced processes are artificially selected on signal-enhancing metasurfaces by controlling the interface between target molecules and the outermost metal surface. To our knowledge, such selective enhancement has not been demonstrated so far, making the metasurface platforms two-way functional and more useful in detecting low-density target molecules in actual sensing configurations.

2. Results and discussion

2.1. Scheme of artificial control of optical transitions

Fig. 1 sums up the optical configurations and processes addressed in this paper. Fig. 1a illustrates a stacked complementary (SC) plasmo-photonic (PlasPh) metasurface based on a silicon-on-insulator (SOI) substrate. FL molecules sparsely dispersed on the SC metasurface are resonantly excited and the emitted optical signals are collected; the setup of the optical measurement was an illumination-collection μ-FL setup, described in the ESI (Fig. S1).† Fig. 1b and c show schematic energy diagrams describing the detected optical signals. A cycle of the optical transitions starts at resonant excitation of the FL molecules *via* HOMO–LUMO transition. The emitted signals were controlled due to the configuration interaction on the SC metasurfaces. As illustrated at the top of Fig. 1b, the molecules are directly placed on the Au surface whereas, in Fig. 1c, a self-assembled monolayer (SAM) shown with green is grown on the Au surface and the target molecules are placed on the SAM with a finite distance from the Au surface. In this study, we used a SAM of 10-carboxy-1-decanethiol (10-CDT, DOJINDO Laboratories, Japan), which forms a sub-nm (approximately 0.6 nm) spacer layer between the molecules and the Au surface; the thickness of the spacer layer was estimated from the length and angle of the C–C chain[29] and from the tilt angle of the chain on the Au surface.[30] The full coverage on the Au surface with the SAM was confirmed by X-ray photoelectron spectroscopy.[31]

The SC structures have unique features in that hybrid resonances of plasmons and photonic guided resonances[32] are formed and high-emittance resonances were employed to realize a large FL-intensity enhancement.[31,33,34] Comparing the thickness of the SC structures with working wavelengths, the thickness is mostly less than the half wavelengths and quite shallow; therefore, we call the structures SC metasurfaces.

In Fig. 1a, typical dimensions of the SC metasurface were as follows: the periodicity of the hexagonal array of air holes was 410.5 nm; the air-hole diameters (*D*) were set at 190 to 314 nm

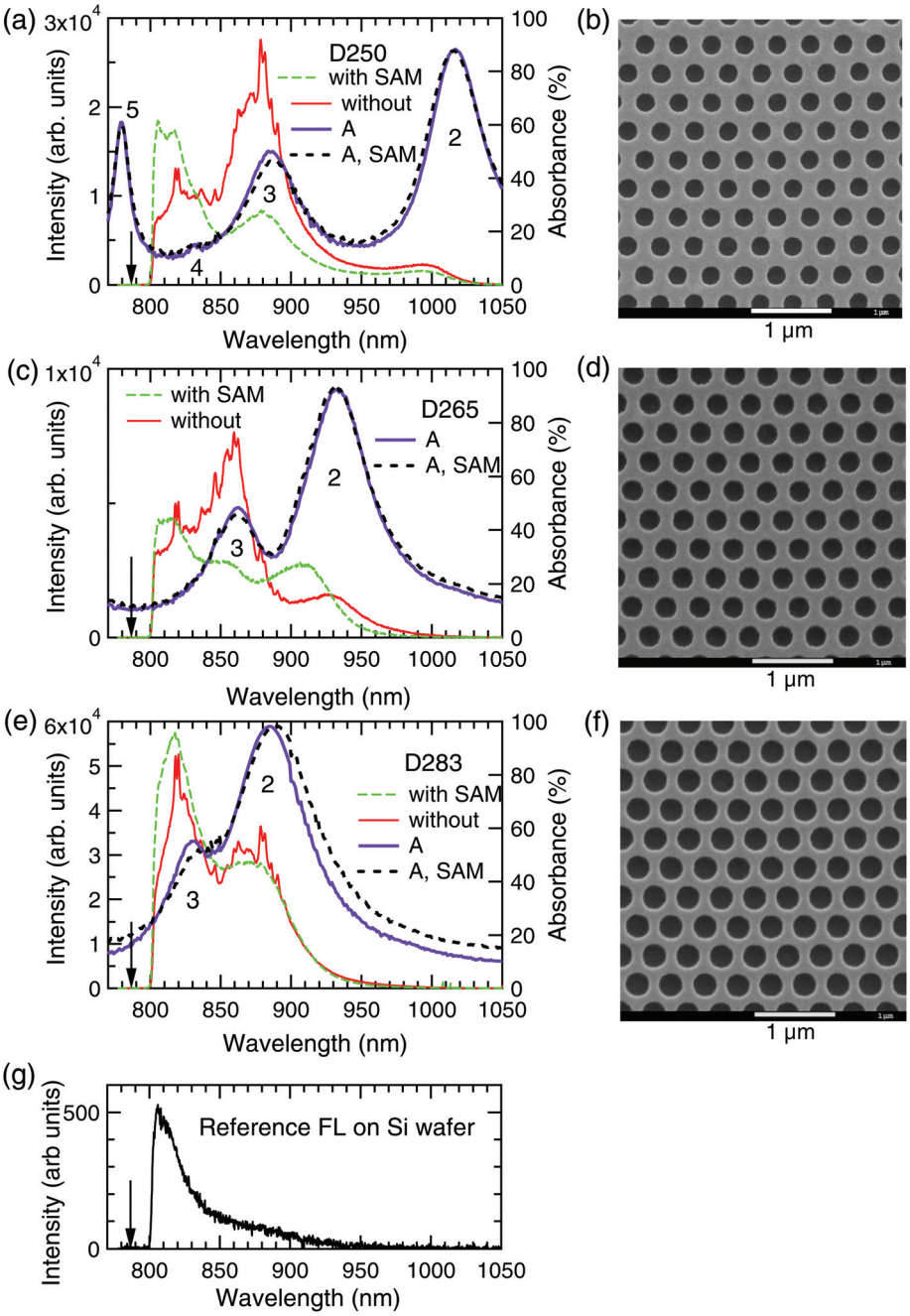

Fig. 2 Measured enhanced optical signals of IR783 molecules dispersed on the SC metasurfaces with/without a SAM. The spectra are shown in a wavelength representation. (a) A set of spectra for air-hole diameter D250 nm, whose top-view SEM image is shown in (b). (c) The spectra for D265 nm; (d) the SEM image. (e) The spectra for D283 nm; (f) the SEM image. Red solid lines in (a), (c) and (e) denote enhanced Raman scattering without SAM; green dashed lines FL-enhanced spectra with SAM. Absorbance *A* spectra of the SC metasurface with and without a SAM are plotted in the right axes, shown with purple solid and black dashed lines, respectively. White scale bars in (b), (d), and (f) denote 1 μm. (g) Reference FL spectrum of IR783 molecules dispersed on a Si wafer, which was measured under an equivalent condition to (a), (c), and (e). Arrows indicate an excitation wavelength of 786.6 nm.

in the experimental samples; the thickness of Au, SOI, and buried oxide (BOX) layers was 35, 200, and 375 nm, respectively. The SC metasurfaces were fabricated by high-throughput UV nanoimprint lithography (NIL) and the dimensions on a SOI substrate were 10 × 10 mm^2 and quite large.[33,34] The procedure of the UV NIL is summarized in the ESI.† Besides, a feature in our procedure and an advantage of reuse are noted in the Method sections.

2.2. Selectively enhanced optical signals

Fig. 2 shows typical sets of enhanced optical signals from near-infrared FL dye molecules, termed IR783 (Sigma-Aldrich,

Inc., USA), whose structure appears later (Fig. 3). The molecules were dispersed on the SC metasurfaces at a low density of less than 1 molecule per 15 × 15 nm^2 on average; the density means that most of the molecules were isolatedly dispersed. As for the molecule density, we note that photo-bleaching substantially reduces the density. Generally, FL molecules are affected by resonant photo-excitation and finally cease to emit FL. In our measurement, the first three-minute photo-irradiation reduced the optical signal intensity to approximately 1/3 of the initial intensity. After that, the intensity remained almost constant for a few minutes; therefore, we measured the optical signals for 20 s after the first three-minute photo-irradiation. Thus, the observed optical signals come from at most 1/3 density of the dispersed density. Also note that we do not include the FL yield of the dispersed molecules, which is inferred to be much smaller than the FL yield in appropriate organic solvents, so that it is likely that the molecule density actually involved in the optical signals is much smaller than the dispersed density.

Fig. 2a and b show the measured optical signals from a SC metasurface of D250 nm and the top-view scanning electron microscopy (SEM) image, respectively. The abscissa of the optical spectra represents the wavelength in nm. Similarly, Fig. 2c and d show the data set of D265 nm, and Fig. 2e and f show the data set of D283 nm. Another set of the SC metasurface of D314 nm is presented in the ESI (Fig. S3).† Also, a set of magnified SEM images of the SC metasurfaces is provided in Fig. S4.†

In Fig. 2, the optical signals from the SC metasurface without any SAM (red solid lines) and with the SAM (green dashed lines) are shown. Evidently, sharp signals corresponding to Raman scattering appear only when the SC metasurfaces are not covered by the SAM. The Raman signals appear around the molecular fingerprint (FP) range from 650 to 1300 cm^{-1} as examined later, exhibiting a Raman band. We also point out that only FL was observed except for the Raman band, that is, in the wavelength range longer than 900 nm, which supports that the IR783 molecules are preserved (or not affected chemically) on the SC metasurfaces. In addition, we mention the relative difference in the optical signal intensity in Fig. 2. This is mainly due to the drops by the pipette used in dispersing the molecules. As is widely known, it is difficult to disperse exactly the same amount of drops using a pipette. In our measurement, we estimated that a few times difference in the intensity could occur. However, we stress that the spectral shapes were reproduced quite well; in this sense, we can state the reproducibility. Related to this point, optical signals are compared and confirmed to be reproduced under similar experimental conditions in Fig. S5.† Furthermore, the optical signals were quite uniform on each SC metasurface; the spot-to-spot measurement resulted in a small signal intensity difference less than 5% as mentioned above.

Fig. 2g shows the reference FL spectrum of IR783 molecules dispersed on a Si wafer. The density of the dispersed molecules was equivalent in Fig. 2 and the measured conditions were also equivalent; however, the measured signal intensities were obviously enhanced on the SC metasurfaces. When

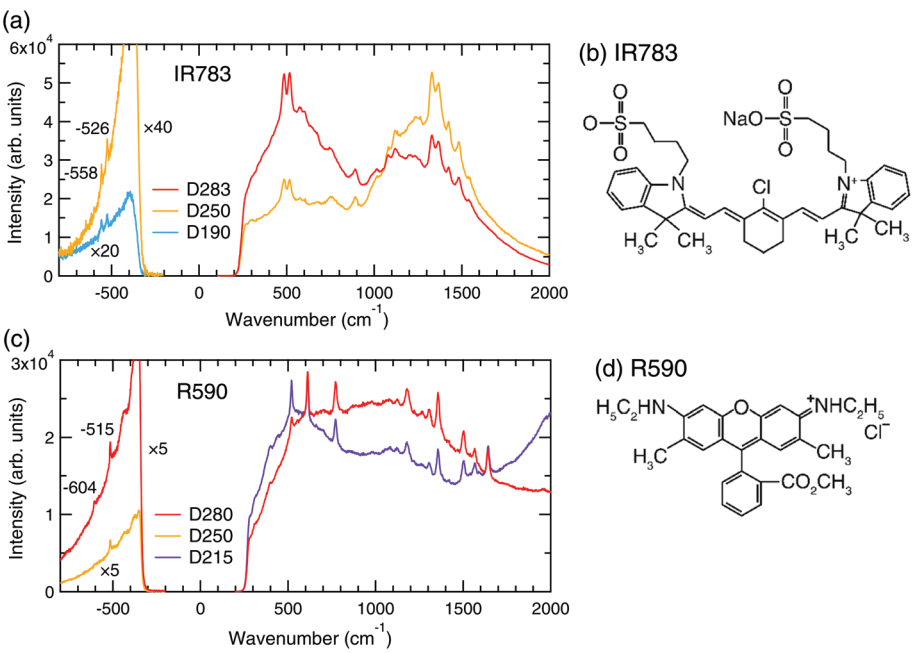

Fig. 3 Representative Raman-scattering enhanced spectra in the wavenumber representation and molecular structures. The FP and anti-Stokes ranges are included. (a) The Raman spectra of IR 783 molecules on the SC metasurfaces of D190 (light blue line), D250 (yellow lines), and D283 (red line). (b) IR783 molecular structure. (c) The Raman spectra of R590 molecules on the SC metasurface of D215 (purple line), D250 (yellow line) and D280 (red lines). (d) R590 molecular structure. The anti-Stokes signals were enlarged for clarity by 5 to 40 times.

compared with the reference FL signals, the signal intensities on the SC metasurfaces are hundred- to thousand-fold larger. Arrows indicate an excitation laser wavelength of 786.6 nm. We used a long-wavelength pass filter to terminate the laser light in the measurement; the resultant sharp edge is located at 800 nm. Besides, we note that the FL intensity in Fig. 2g was maximum in several measurements for the reference configuration. This is probably due to the handling of the pipette as described above.

In Fig. 2, absorbance (A) spectra of the SC metasurfaces are plotted in the right axis. The A in the linear optical response is evaluated by

$$A = 100 - R - T - \mathrm{DF} \quad (1)$$

in % where measurable optical quantities R, T, and DF denote reflectance, transmittance, and total diffraction, respectively. For the SC metasurfaces, T and DF are zero or negligible; therefore we set the two terms to be 0 in eqn (1). The A spectra shown with purple lines were evaluated based on the measured R spectra of the SC metasurfaces without a SAM and the A spectra shown with black dashed lines based on the SC metasurfaces with a SAM. The two-type SC metasurfaces exhibit quantitatively almost equivalent A spectra and indicate that the SAM hardly affects the optical properties of the metasurface. The numbers from 2 to 5 in Fig. 2a denote the second to fifth resonances of the SC metasurfaces at the normal incidence; the numbers of 2 and 3 in Fig. 2c and e are shown with a similar meaning. The A spectra were measured at an incident angle of 5° and were almost same to those at the normal incidence; the plane of incidence was the xz plane in Fig. 1a and the polarization E_{in} was set to the $E_{\mathrm{in}} \| xz$ plane.

We mention that Kirchhoff's radiation law tells us that the absorbance A of structured surfaces is equal to the emittance.[35] Indeed, the enhanced spectra have local maxima in accordance with the peaks of A spectra. We note that the Raman band is particularly enhanced by the third resonance of the SC metasurfaces and becomes dominant as shown with the red lines in Fig. 2a and c, exceeding the FL component. We are able to estimate the Raman-scattering signals for more than 10 000 counts at the maximum in Fig. 2c when we simply assume a smooth enveloping of the FL component. On the other hand, the reference signal in Fig. 2g shows that Raman-scattering signals are under the detection limit, that is, less than 5 counts, taking into account the signal-to-noise ratio in the measurement. Therefore, the Raman-scattering signals are estimated to be more than 2000 fold at the maximum on the SC metasurfaces. The second resonance, which is connected to nearly perfect emittance, induces a large FL-intensity enhancement up to thousand fold (for example, 1400 fold at 1000 nm in Fig. 2a) for the reference signals while it less significantly enhances the Raman band than the third resonance. These results imply that the details of the resonance of the SC metasurfaces play a key role in the prominent Raman-scattering enhancement.

In addition to the significant signal-enhancing capability and the uniform responses, we also point out that the resonances in the SC metasurfaces are tunable by varying the air-hole diameters and fully cover the FP range. This tunability is advantageous in on-demand enhanced spectroscopy.

Raman-scattering enhanced signals on the SC metasurfaces were also measured for rhodamine 590 chloride (R590, Exciton, Inc., USA) molecules (ESI, Fig. S6†), which have been frequently used for the SERS experiment since the 1980s.[15,16] The Raman signals were detected mainly around the FP range, similarly to IR783 in Fig. 2.

We here mention the effect due to the thickness of the SAM layer. Fig. 2 and S6† show the result using 10-CDT molecules. We already employed 5-carboxy-1-pentathiol (5-CPT) and 15-carboxy-1-pentadecanethiol (15-CPDT).[31,34] The former and latter form 0.3 and 0.9 nm spacer layers on the Au surface, respectively. The thickness of the 5-CPT is comparable to the atomic-scale roughness of the deposited Au surface, being found to be not enough to the suppress FL quenching of R590 molecules.[31] On the other hand, the 15-CPDT spacer layer induced FL-dominant optical signals for IR783 molecules,[34] just as the case with a SAM of 10-CDT in Fig. 2. Thus, we are able to select the two enhanced optical signals (that is, FL and Raman scattering) with/without the SAM thicker than the SAM of 10-CDT.

2.3. Details of Raman lines

Fig. 3 shows Raman-scattering enhanced spectra in a wavenumber representation, including the FP range on the Stokes side and a range on the anti-Stokes side of negative wavenumbers. Fig. 3a and b show the signals from IR783 and the molecular structure, respectively. The spectra obviously include several prominent Raman peaks on the Stokes side: 487, 518, 575, 745, 891, 1017, 1080, 1119, 1330, 1364, 1424, 1480, and 1540 cm^{-1}. As for IR783 molecules, although the vibration modes have not been identified to our knowledge, most of the signals belong to the typical C–C stretch band at 700–1250 cm^{-1} and the C–H band at 1340–1465 cm^{-1}.[29] The anti-Stokes signals were observed at −526 and −558 cm^{-1}.

Fig. 3c and d show those from R590 molecules on the SC metasurfaces without a SAM and the molecular structure, respectively. In Fig. 3c, several Raman peaks were observed at 521, 614, 773, 1364, 1509, 1573, and 1651 cm^{-1}. As for R590 molecules, many SERS studies have been reported so far; for example, the 522 cm^{-1} line was assigned to torsion and/or bending of the ring, the 614 cm^{-1} to the C–C–C in-plane bending mode, the 773 cm^{-1} to the C–H out-of-plane bending mode, and the 1364, 1509, and 1651 cm^{-1} to aromatic C–C stretching modes.[15] The anti-Stokes signals were detected at −515 and −604 cm^{-1}.

Thus, the enhanced Raman signals on the SC metasurfaces provide information on the molecules around the FP range. Actually, IR783 and R590 yield different Raman signals that represent the molecule characters. Note that the Stokes-side spectra in Fig. 3 were displayed as equal at the maxima. Anti-Stokes Raman-scattering signals were detected in the range

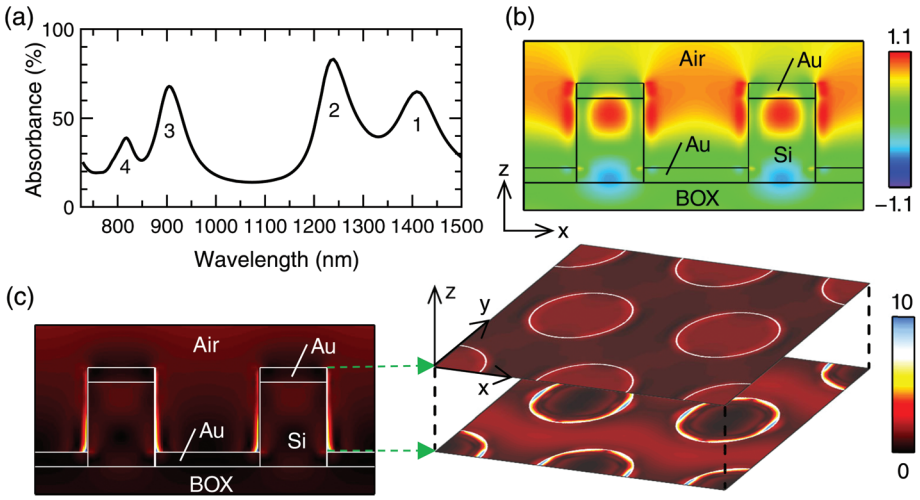

Fig. 4 Numerically calculated EM-field distributions at the third resonance of 904.8 nm. (a) *A* spectrum of the SC metasurface of D250 at the normal incidence. Numbers 1 to 4 indicate the first to fourth resonances, respectively. (b) Snapshot of the *x* component of the *E*-field distribution at an *xz* section through centers of air holes. (c) Absolute value of the *E* field, $|\mathbf{E}|$, at the *xz* section same to (b). The *xy* sections are also shown at the *z* positions indicated by green dashed arrows. Incidence was set to have $|\mathbf{E}_{in}| = 1.0$.

from −500 to −600 cm^{-1} where a shorter wavelength tail of the FL appears simultaneously. The anti-Stokes signals are also enhanced in accordance with the high emittance of the SC metasurfaces. Note that the signals are enlarged by 5 to 40 times to clearly present the anti-Stokes signals. We mention that the absorbance spectra of the SC metasurfaces of D190 and D280 are obtained for the anti-Stokes range (not shown), using eqn (1) and the measured *R* spectra are shown in Fig. S2.†

2.4. Resonant EM fields on a SC metasurface

Fig. 4 shows numerically calculated electromagnetic (EM) field distributions at the third resonance of the SC metasurface of D250 nm; the resonance was found to especially contribute to Raman-scattering enhancement in Fig. 2. Fig. 4a shows the computed *A* spectrum, which was evaluated by eqn (1). The numbers 1 to 4 in Fig. 4a mean the first to fourth resonances induced at the normal incidence of *x* polarization. The coordinate was set in Fig. 4b and c; the *xz* section includes the centers of air holes in the SC metasurface.

Fig. 4b and c show a snapshot of the *E*-field *x* component, $\mathrm{Re}(E_x)$, and the absolute value of the *E* field, $|\mathbf{E}|$, respectively; the incident wavelength is 904.8 nm. Two *xy* sections are also shown in Fig. 4c, which are located at the top of the SC metasurface and at the bottom of the air holes as indicated by green dashed arrows. Fig. 4c is displayed at (0, 10) range for clarity though the maximum value in Fig. 4c is 14.1 where the incident *E* field $\mathbf{E}_{in}$ was set to be $|\mathbf{E}_{in}| = 1.0$. The maximum value mostly comes from the E_z component. The hot spots of the *E* field appear near the rim of the Au disk at the bottom and therefore some of the molecules located at the bottom are likely to be assisted by the *E*-field distribution, though the hot spots are limited to a small portion on the SC metasurface and most of the outermost surface has small $|\mathbf{E}|$ values less than 2. Thus, the *E*-field enhancement is limited to one of the contributing factors for the significantly enhanced signals in Fig. 2, because most of the dispersed molecules are not considered to be located at the hot spots. We can use the previous estimations[31,34] that take into account the *E*-field distributions at the excitation wavelengths; the estimation concluded at most several-fold *E*-field enhancement on average.

The calculations for the spectrum and EM fields in Fig. 4 were implemented based on rigorous coupled-wave analysis (RCWA)[36] and the scattering (*S*) matrix method,[37] whose details are noted in the Method section. To implement realistic calculations, constituent material parameters of permittivity were taken from the literature.[38,39] Systematic numerical *A* spectra for the SC metasurface with various D are shown in the ESI (Fig. S7†). In addition, the *E*-field distributions on the second resonance in Fig. 4a are also shown in the ESI (Fig. S8†).

2.5. Comparison with a previous result

Let us discuss the present results by comparison with the previous result on the FL enhancement of R590 molecules with the SAM.[31] We first point out that we focused on a range except for the FP range in the previous study; then, the FL was the focused issue. Second, R590 molecules are nearly ideal FL emitters and the quantum yield of the FL is almost 100% in organic solvents; as a result, it was found that the R590 molecules on the SAM-coated SC metasurface exhibit a suppression of FL quenching, in other words, a substantial increase in the FL intensity.

In contrast, IR783 molecules do not have such a large quantum yield even when they are in organic solvents; therefore, it is plausible that the FL intensity from the SAM-coated SC metasurfaces in Fig. 2 is not substantially larger than the FL intensity from the SC metasurfaces without SAM, because

of the inner nonradiative transitions. The Raman signals from IR 783 molecules were found to become prominent when the FP range is tuned on a suitable PlasPh resonance as shown in Fig. 2. This result suggests that a part of the nonradiative transitions is switched into the Raman process and becomes the enhanced Raman signals.

2.6. Underlying mechanism of the optical-transition change

As for the change in the enhanced optical transitions, we here consider a few possible origins. Information obtained from the experimental data is schematically summarized in Fig. 1b and c. The configuration interaction of FL molecules with PlasPh resonances changes the transitions in a qualitative manner. The difference in the configuration is ascribed only to whether direct contact of the metal and molecules takes place or not. Fig. 5 illustrates energy diagrams and possible underlying mechanisms in a weak coupling regime of the FL molecules and PlasPh resonances; note that the possible dynamics takes place just after the resonant excitation of the FL molecule *via* the HOMO–LUMO transition and is an ultrafast phenomenon.

Fig. 5a shows the excitation-energy transfer (red zigzag arrow) in the case of the SC metasurfaces without a SAM, on which the dispersed FL molecules directly contact the Au outmost surface. Then, it is first inferred that metal-induced FL quenching takes place;[40] however, such drastic FL quenching was not observed for IR783 as shown in Fig. 2 and S3 (ESI†). Instead, the prominent Raman signals were observed.

Related to the configuration of the direct molecule–metal contact in Fig. 5a, the first layer model[41] was proposed to describe the origin of SERS. The model assumed that the excitation energy transfer moves the excited electron to an intermediate state and its succeeding scattering by the metallic surface of atomic-scale roughness results in Raman signals; that is, the model assumed a second-order transition. However, the excitation energy transfer is a first-order transition, which was not observed clearly in the experimental results (Fig. 2 and S3†). Generally, it is quite unlikely that a second-order effect is more prominent than a first-order effect. Thus, the first layer model is not suitable in this case. We point out that the model was proposed for non-FL molecules and therefore assumed much simpler cases than the present case involving FL and Raman processes. Overall, we do not believe that the excitation transfer and the first layer model are able to describe the underlying mechanism of the FL/Raman selection.

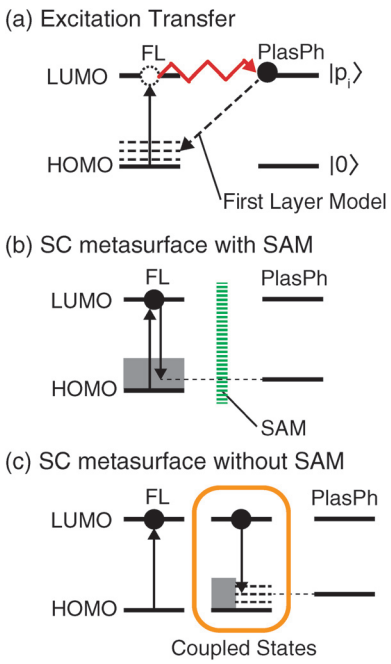

Fig. 5 Schematics of the possible underlying mechanism on the SC metasurfaces, which take place just after the initial excitation in the FL molecule. Energy diagrams are drawn in the weak-coupling regime. (a) Excitation energy transfer from LUMO to the metasurface (red zigzag arrow) for the case without a SAM. Besides, the first layer model, which adds scattering on the Au surface of atomic-scale roughness (black dashed arrow), is also included. The final states are vibrational levels (black broken lines) in FL molecules. (b) and (c) Energy diagrams of FL molecules on the SC metasurfaces with and without a SAM, respectively. In (b), the SAM (green) separates the FL states from the PlasPh resonances. In (c), coupled states inside the yellow solid line result from the weak coupling of the molecular states and PlasPh resonances.

Fig. 5b shows energy diagrams of FL molecules on the SC metasurfaces with a SAM (green), which separates the FL states and PlasPh resonances. Under this situation, the final states are located in the FL band (gray) and the resultant emission signals are dominantly FL because the SAM plays a role in making the FL molecules remain electronically isolated. When the emission wavelength is matched to a PlasPh resonance in energy, as indicated by a thin dashed line, the FL is particularly enhanced as observed in Fig. 2 and S3.†

Fig. 5c shows the energy diagrams of FL molecules on the SC metasurfaces without a SAM. If vibrational levels are activated, the prominent Raman signals in Fig. 2 and S3† are accountable. In terms of the energy diagram, such a situation is understood as the formation of coupled states, surrounded by a yellow line in Fig. 5c, due to the configuration interaction of the FL molecule with the PlasPh resonances. The FL band (gray) also remains in part, contributing to the emission signals. The coupled states seem to be plausible though it is not obvious at present whether the activated vibrational levels are formed in a static or dynamic way.

In configurations where molecules or emitters directly contact metallic surfaces, a substantial increase in the nonradiative decay rate was frequently reported.[42,43] A decay-time study concluded that the nonradiative decay time is about 25 fs,[43] suggesting a dominant nonradiative decay on the ultrafast time scale. However, the measured optical signals were increased in this study; therefore, it is unlikely that nonradiative processes become dominant on the SC metasurfaces without a SAM. This supports that the SC metasurface is suitable for molecular sensing platforms. The large optical-signal enhancement probably allows us to access a very low detection limit of molecules, as demonstrated in Si photonic crystal slabs.[44]

3. Conclusions

We fabricated several large-area SC PlasPh metasurfaces by UV NIL in a high-throughput way; the SC metasurfaces meet on-demand enhancing spectroscopy owing to the working wavelength tunability and the highly enhancing capability. We clearly observed two distinct enhanced optical signals from the FL molecules on the interface-controlled SC metasurfaces. The two processes were found to be artificially selectable by controlling the metal–molecule interface with sub-nm precision, suggesting that the electronic states in the FL molecules are substantially modified due to the configuration interaction. Moreover the enhanced Raman-scattering signals were detected in a wavenumber range including the FP range, providing useful information to identify target molecules. The FL and Raman-scattering signals were detected efficiently and uniformly on the SC metasurfaces in a sensing configuration. These experimental results demonstrate that the SC metasurfaces are highly practical as molecular sensing platforms.

4. Method

4.1. UV NIL with lateral tunability

Several SC PlasPh metasurfaces of different air-hole diameters were employed in this study. The whole procedure was a standard UV NIL as noted in the ESI.† Still, it is to be noted that the SC metasurfaces were fabricated using only one quartz mold that has a pillar array of a fixed diameter. The lateral tuning of the structures was made possible by introducing a slow-rate removal of the residual thin film with O_2 + N_2 plasma.[34] We were able to obtain the different diameters with approximately 5 nm precision through the slow-rate treatment. The lateral tuning makes UV NIL more practical because it enables us to reduce the cost for the molds.

4.2. Reuse of the SC metasurfaces

UV NIL produced perforated patterns on SOI substrates. The SC metasurfaces were obtained after Au deposition on the patterned SOI substrates. This simple procedure of the metal has advantages in yielding good-quality Au in the SC structures and in the easy reuse of the SC metasurfaces with the repeated removal of Au and its deposition. Note that, even after the SAM was grown, the removal of Au was easily done.[31] Indeed, we reused the nanoimprinted SOI substrates repeatedly in a series of experiments. Thus, the SC metasurfaces are advantageous in actual applications. We point out that this kind of reuse is hard in most of the highly enhancing plasmonic platforms because the metallic nanostructures have to be produced from the beginning for the next fresh use.

4.3. Numerical method to compute EM fields on metasurfaces

RCWA is an established numerical technique to directly solve Maxwell equations for periodic structures in a precise manner.[36] An arbitrary in-plane periodic layer has eigenmodes due to the periodic structure and is described by the Fourier-transformed Maxwell equations. RCWA was conceived to numerically compute the eigenmodes in a rapidly converging manner. RCWA has a definite advantage in handling periodic systems including lossy materials like metals. In each layer, the *xy* plane defined in Fig. 1a was divided by 2×2 nm^2 grids.

The SC metasurfaces have three-periodic-layer stacked structures and therefore need to combine the three eigenmode series. Such a combination is implemented by the *S*-matrix algorithm,[37] which ensures numerical stability. Eigenmodes in each layer are combined through the *S*-matrix algorithm. The total optical responses of the SC metasurfaces such as reflectance and transmittance were evaluated for the given incident plane waves.

At optical wavelengths of present interest, permittivity is the key material parameter in Maxwell equations; the permittivity of Au was taken from the literature,[38] that of Si from another literature,[39] and those of air and SiO_2 were set to 1.00054 and 2.1316, respectively. We implemented the computations using our own code on supercomputers in a multi-parallel way.

Acknowledgements

This study was partially supported by the third mid-term research project "Innovative Photonic Materials" in NIMS and by a Grant-in-Aid for Innovative Research Area (number 22109007) from the Ministry of Education, Culture, Sports, Science and Technology, Japan. M. I. acknowledges the financial support by a Grant-in-Aid (number 26706020) from the Japan Society for the Promotion of Science and the support in numerical implementations by the Cyberscience Center, Tohoku University and Cybermedia Center, Osaka University through HPCI System Research Project (ID: hp150043), Japan. Nanofabrication and the characterization were conducted at NanoIntegration Foundry and Low-Carbon Network in NIMS.

References

1 A. Furube, L. Du, K. Hara, R. Katoh and M. Tachiya, *J. Am. Chem. Soc.*, 2007, **129**, 14852–14853.
2 P. Christopher, H. Xin, A. Marimuthu and S. Linic, *Nat. Mater.*, 2012, **11**, 1044–1050.
3 S. Mubeen, J. Lee, N. Singh, S. Krämer, G. D. Stucky and M. Moskovits, *Nat. Nanotechnol.*, 2013, **8**, 247–251.
4 K. Wu, J. Chen, J. R. McBride and T. Lian, *Science*, 2015, **349**, 632–635.
5 M. Fleischmann, P. J. Hendra and A. J. McQuillan, *Chem. Phys. Lett.*, 1974, **26**, 163–166.
6 D. L. Jeanmaire and R. P. van Duyne, *J. Electroanal. Chem.*, 1977, **84**, 1–20.
7 M. G. Albrecht and J. A. Creighton, *J. Am. Chem. Soc.*, 1977, **99**, 5215–5217.
8 A. M. Glass, P. F. Liao, J. G. Bergman and D. H. Olson, *Opt. Lett.*, 1980, **5**, 368–370.

9 A. Otto, I. Mrozek, H. Grabhorn and W. Akemann, *J. Phys.: Condens. Matter*, 1992, **4**, 1143–1212.
10 S. Nie and S. R. Emory, *Science*, 1997, **275**, 1102–1106.
11 K. Kneipp, Y. Wang, H. Kneipp, L. T. Perelman, I. Itzkan, R. R. Dasari and M. S. Feld, *Phys. Rev. Lett.*, 1997, **78**, 1667–1670.
12 J. R. Lakowicz, K. Ray, M. Chowdhury, H. Szmacinski, Y. Fu, J. Zhang and K. Nowaczyk, *Analyst*, 2008, **133**, 1308–1348.
13 M. Bauch, K. Toma, M. Toma, Q. Zhang and J. Dostalek, *Plasmonics*, 2014, **9**, 781–799.
14 L. Chen, Y. Gao, Y. Cheng, H. Li, Z. Wang, Z. Li and R.-Q. Zhang, *Nanoscale*, 2016, **8**, 4086–4093.
15 P. Hildebrandt and M. Stockburger, *J. Phys. Chem.*, 1984, **88**, 5935–5944.
16 Y. Maruyama and M. Futamata, *Chem. Phys. Lett.*, 2007, **448**, 93–98.
17 W.-D. Li, F. Ding, J. Hu and S. Y. Chou, *Opt. Express*, 2011, **19**, 3925–3936.
18 S. Mubeen, S. Zhang, N. Kim, S. Lee, S. Krämer, H. Xu and M. Moskovits, *Nano Lett.*, 2012, **12**, 2088–2094.
19 H. Aouani, H. Šípová, M. Rahmani, M. Navarro-Cia, K. Hegnerová, J. Homola, M. Hong and S. A. Maier, *ACS Nano*, 2013, **7**, 669–675.
20 Y. Shen, T. He, W. Wang, Y. Zhan, X. Hu, B. Yuan and X. Zhou, *Nanoscale*, 2015, **7**, 20132–20141.
21 S. E. J. Bell and N. M. S. Sirimuthu, *Chem. Soc. Rev.*, 2008, **37**, 1012–1024.
22 J. F. Li, Y. F. Huang, Y. Ding, Z. L. Yang, S. B. Li, X. S. Zhou, F. R. Fan, W. Zhang, Z. Y. Zhou, D. Y. Wu, B. Ren, Z. L. Wang and Z. Q. Ti, *Nature*, 2010, **464**, 392–395.
23 J. Li, C. Chen, H. Jans, X. Xu, N. Verellen, I. Vos, Y. Okumura, V. V. Moshchalkov, L. Lagae and P. Van Dorpe, *Nanoscale*, 2014, **6**, 12391–12396.
24 J. Li, C. Chen, H. Jans, X. Xu, N. Verellen, I. Vos, Y. Okumura, V. V. Moshchalkov, L. Lagae and P. Van Dorpe, *Nanoscale*, 2016, **8**, 5928–5937.
25 Y. Wang, B. Yan and L. Chen, *Chem. Rev.*, 2013, **113**, 1391–1428.
26 L. A. Lane, X. Qian and S. Nie, *Chem. Rev.*, 2015, **115**, 10489–10529.
27 W. Zhang, F. Ding, W.-D. Li, Y. Wang, J. Hu and S. Y. Chou, *Nanotechnol.*, 2012, **23**, 225301.
28 L. Zhou, F. Ding, H. Chen, W. Ding, W. Zhang and S. Y. Chou, *Anal. Chem.*, 2012, **84**, 4489–4495.
29 P. Atkins and J. de Paula, *Physical Chemistry*, Oxford Univ. Press, Oxford, UK, 9th edn, 2010.
30 J. C. Love, L. A. Estroff, J. K. Kriebel, R. G. Nuzzo and G. M. Whitesides, *Chem. Rev.*, 2005, **105**, 1103–1170.
31 B. Choi, M. Iwanaga, H. T. Miyazaki, Y. Sugimoto, A. Ohtake and K. Sakoda, *Chem. Commun.*, 2015, **51**, 11470–11473.
32 M. Iwanaga and B. Choi, *Nano Lett.*, 2015, **15**, 1904–1910.
33 B. Choi, M. Iwanaga, H. T. Miyazaki, K. Sakoda and Y. Sugimoto, *J. Micro/Nanolithogr., MEMS, MOEMS*, 2014, **13**, 023007.
34 M. Iwanaga, B. Choi, H. T. Miyazaki, Y. Sugimoto and K. Sakoda, *J. Nanomater.*, 2015, **2015**, 507656.
35 J.-J. Greffet and M. Nieto-Vesperinas, *J. Opt. Soc. Am. A*, 1998, **15**, 2735–2744.
36 L. Li, *J. Opt. Soc. Am. A*, 1997, **14**, 2758–2767.
37 L. Li, *J. Opt. Soc. Am. A*, 1996, **13**, 1024–1035.
38 A. D. Rakić, A. B. Djurišić, J. M. Elazar and M. L. Majewski, *Appl. Opt.*, 1998, **37**, 5271–5283.
39 E. D. Palik, *Handbook of Optical Constants of Solids II*, Academic, San Diego, USA, 1991.
40 R. R. Chance, A. Prock and R. Silbey, *Adv. Chem. Phys.*, 1978, **37**, 1–65.
41 A. Otto, *Phys. Status Solidi A*, 2001, **188**, 1455–1470.
42 P. Anger, P. Bharadwaj and L. Novotny, *Phys. Rev. Lett.*, 2006, **96**, 113002.
43 C. M. Galloway, P. G. Etchegoin and E. C. Le Ru, *Phys. Rev. Lett.*, 2009, **103**, 063003.
44 B. Choi, M. Iwanaga, T. Ochiai, H. T. Miyazaki, Y. Sugimoto and K. Sakoda, *Appl. Phys. Lett.*, 2014, **105**, 201106.